

Segmentation, Splitting, and Classification of Overlapping Bacteria in Microscope Images for Automatic Bacterial Vaginosis Diagnosis

Youyi Song, Liang He, Feng Zhou, Siping Chen, Dong Ni, Baiying Lei*, and Tianfu Wang*

Abstract—Quantitative analysis of bacterial morphotypes in the microscope images plays a vital role in diagnosis of bacterial vaginosis (BV) based on the Nugent score criterion. However, there are two main challenges for this task: 1) It is quite difficult to identify the bacterial regions due to various appearance, faint boundaries, heterogeneous shapes, low contrast with the background, and small bacteria sizes with regards to the image. 2) There are numerous bacteria overlapping each other, which hinder us to conduct accurate analysis on individual bacterium. To overcome these challenges, we propose an automatic method in this paper to diagnose BV by quantitative analysis of bacterial morphotypes, which consists of a three-step approach, i.e., bacteria regions segmentation, overlapping bacteria splitting, and bacterial morphotypes classification. Specifically, we first segment the bacteria regions via saliency cut, which simultaneously evaluates the global contrast and spatial weighted coherence. And then Markov random field model is applied for high-quality unsupervised segmentation of small object. We then decompose overlapping bacteria clumps into markers, and associate a pixel with markers to identify evidence for eventual individual bacterium splitting. Next, we extract morphotype features from each bacterium to learn the descriptors and to characterize the types of bacteria using an Adaptive Boosting machine learning framework. Finally, BV diagnosis is implemented based on the Nugent score criterion. Experiments

demonstrate that our proposed method achieves high accuracy and efficiency in computation for BV diagnosis.

Index Terms—Automatic bacterial vaginosis diagnosis, bacteria segmentation, bacterial morphotypes recognition, overlapping bacteria splitting, saliency cut.

I. INTRODUCTION

BACTERIAL vaginosis (BV) is a perturbation of vaginal flora characterized by reduced levels of lactobacilli and overgrowth of *Gardnerella*, *Prevotella*, *Mobiluncus*, and other anaerobic bacteria species, which affects nearly 1 in 3 reproductive-age women worldwide [1]. BV is also associated with numerous adverse outcomes, including increased human immunodeficiency virus transmission, spontaneous abortion, and premature delivery among pregnant women [2]. Since BV is often asymptomatic in about 50% of women [3], microbiological-based diagnostic methods, such as Nugent's scoring system, are preferred in the scientific community [4].

The Nugent score is a Gram staining scoring system to diagnose BV [4], which is calculated by assessing the presence of large Gram-positive rods (*Lactobacillus* morphotypes), small Gram-variable rods (*Gardnerella* morphotypes), and curved Gram-variable rods (*Mobiluncus* morphotypes). Table I presents the Nugent score criterion, and a score of 7–10 is consistent with BV. However, the current clinical standard for Nugent score criteria is performed by microscopists. This is a laborious task and a vast amount of data cannot be analyzed effectively. In addition, there is a huge variability of diagnosis result due to the lack of quantifiable analysis of bacteria morphotypes [5], [6], [35].

Therefore, a tool of automatic diagnose BV is desired. The literature of this task mainly focuses on two stages: object regions segmentation and overlapping objects splitting. For object regions segmentation, popular methods include thresholding [7], adaptive thresholding [8], watershed transform [9], and learning techniques, including machine learning [10]–[12], [35] and deep learning [13], [14], and active contour model [15]. However, the single thresholding method [7] does not work well even when the threshold is manually adjusted to the heterogeneous background. And the adaptive thresholding methods [8] are unable to segment overlapping bacteria clumps, for the intensity at the boundary between overlapping bacteria tends to exceed the local threshold. Also, the watershed methods [9] usually produce results that are oversegmented. Learning techniques [10]–[14], [35] require many manual

Manuscript received December 8, 2015; revised March 29, 2016 and June 2, 2016; accepted July 15, 2016. Date of publication July 27, 2016; date of current version June 29, 2017. This work was supported partly by National Natural Science Foundation of China under Grant 81571758, Grant 61571304, Grant 61402296, and Grant 61427806, in part by National Key Research and Develop Program (No. 2016YFC0104703), in part by Guangdong Medical Grant (No. B2016094), in part by Shenzhen Peacock Plan (No. KQTD2016053112051497), in part by Shenzhen Key Basic Research Project (No. JCYJ20150525092940986 and JCYJ20150525092940988), and in part by the National Natural Science Foundation of Shenzhen University (No. 827000197). (Corresponding author: Baiying Lei and Tianfu Wang).

Y. Song, S. Chen, D. Ni, B. Lei, and T. Wang are with National-Regional Key Technology Engineering Laboratory for Medical Ultrasound, Guangdong Key Laboratory for Biomedical Measurements and Ultrasound Imaging, School of Biomedical Engineering, Shenzhen University, Shenzhen 518060, China (e-mail: vigorsony-ouyi@163.com; chensiping@szu.edu.cn; nidong@szu.edu.cn; leiby@szu.edu.cn; tfwang@szu.edu.cn).


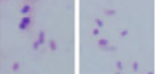
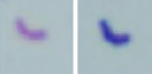
L. He is with the Department of Infectious Diseases, Shenzhen Sixth People's Hospital, Shenzhen 518052, China (e-mail: lianghe@mail.im.ac.cn).

F. Zhou is currently an Assistant Professor at the Department of Industrial and Manufacturing Systems Engineering, The University of Michigan, Dearborn, MI 48128, USA (e-mail: fezhou@umich.edu).

Digital Object Identifier 10.1109/JBHI.2016.2594239

TABLE I

NUGENT SCORE CRITERION (n SCORE = SUM OF THE SCORES FOR EACH BACTERIAL MORPHOTYPE LISTS BELOW. NOTE THAT NUMBER OF ORGANISM IS OBSERVED BY $100 \times$ OBJECTIVE)

Nugent Score	Lactobacillus morphotypes	Gardnerella morphotypes	Mobiluncus morphotypes
			
0	>30	0	0
1	5~30	<1	1~5
2	1~4	1~4	>5
3	<1	5~30	N/A
4	0	>30	N/A

decisions and intermediate steps. Active contour models [15] are too time-consuming in the energy optimization, especially when the image has a large number of objects.

Meanwhile, the widely used methods to split overlapping bacteria clumps include watershed and its variants [16], [17], active contour model [18], [19], concave points methods [20], [21], and sliding band filter (SBF) [22]. Although the watershed methods [16], [17] generally can obtain a good result, these methods cannot provide any information on the overlapping-parts. Active contour models [18], [19] are too computationally intensive when handling numerous objects, and the shape prior constraint is too hard to model because of the heterogeneous bacterium shapes. In addition, the concave-points-based methods [20], [21] are limited in its applications as overlapping objects often have no concave points. The SBF method [22] requires prior knowledge of the range of object size, and this method tends to be ineffective and produces oversegmented results for overlapping objects with different sizes.

Moreover, there are still a myriad of challenges in automating BV diagnosis. We illustrate this with Fig. 1, which presents microscope images from four different slides. It is clear that there are many microstructures, especially for the Gardnerella morphotype, and locating these structures is a highly challenging task due to the high variation of shape, faint boundaries, and non-homogenous backgrounds. In addition, there are various overlapping bacteria in microscope images, and these overlapping bacteria prevent accurate analysis of the individual bacterium. Furthermore, BV is a biofilm-associated disorder, so splitting overlapping bacteria is the biggest challenge for BV diagnosis. Theoretically, to differentiate the bacteria in biofilm is pretty difficult and even impossible [36]. Last but not least, there are 100–400 bacteria in a typical image, which make developing a computationally efficient approach for real-time implementation difficult.

To address these challenges, we propose a quantitative analysis of the bacterial morphotypes approach to diagnose BV in this paper. We shall focus on segmenting individual bacterium using two distinct steps, and learning bacteria' morphotypes:

- 1) *Bacteria Regions Segmentation*: We simultaneously evaluate global contrast and spatial weight coherence, which is not only effective in the large image size but also loses

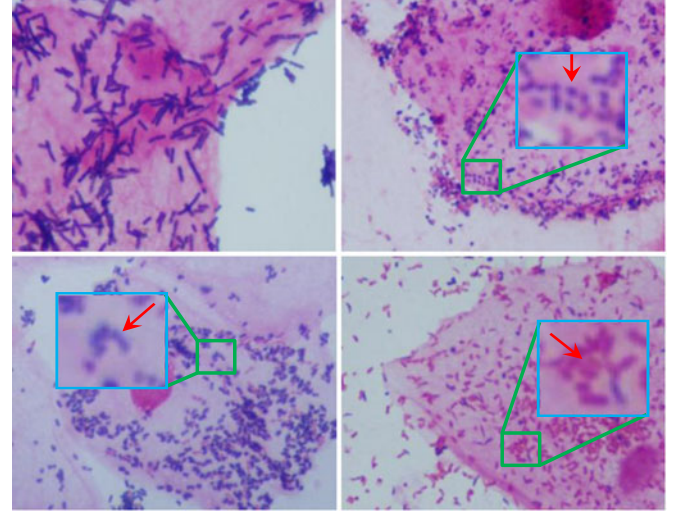


Fig. 1. Illustration of challenges of automated BV diagnosis using four examples of view images. The first challenge is the large number of bacteria in image, which increases the computational complexity. The second challenge is the small size of bacteria as compared to the image size, which makes detecting object regions difficult. The third challenge is that there are many overlapping bacteria, which have low contrast with background, faint boundaries, and large variations in shapes. Therefore, quantitative analysis of each bacterium is not directly permitted (note that images are 1360×1024 pixels and are resized for improved visibility).

fine details of small structures. Then, we apply a Markov random field (MRF) model to incorporate global understanding for unsupervised segmentation of a small object.

- 2) *Overlapping Bacteria Clumps Splitting*: We first decompose the overlapping bacteria clumps into markers, which correspond to bacterium locations. These markers are obtained by enhancing the bacterial rod-like shape features using eigenvalues of Hessian matrices. The remained pixels of clump are then associated with each individual marker according to a compound measure, which makes them meaningful chunks of evidence to delineate individual bacteria.
- 3) *Bacteria' Morphotypes Learning*: We first extract the shape features from each bacterium, and then learn these features by a machine learning framework to classify bacterial morphotypes. Finally, BV diagnosis is implemented according to Nugent score criteria.

The rest of this paper is organized as follows. In Section II, we introduce our approach for automatically diagnose BV. We describe the experimental design and provide the results in Section III. Finally, discussions and conclusion are drawn in Section IV and Section V, respectively.

II. METHODOLOGY

The proposed method consists of three consecutive main steps: bacteria regions segmenting, overlapping clumps splitting, and BV diagnosis based on the learned bacterium morphotypes. Fig. 2 illustrates the proposed method. Selecting certain images of each subject as input, proposed method starts to group pixels into superpixels, and then the saliency value of each superpixel is computed. Next, the bacteria regions are obtained by the MRF model, which is constructed on

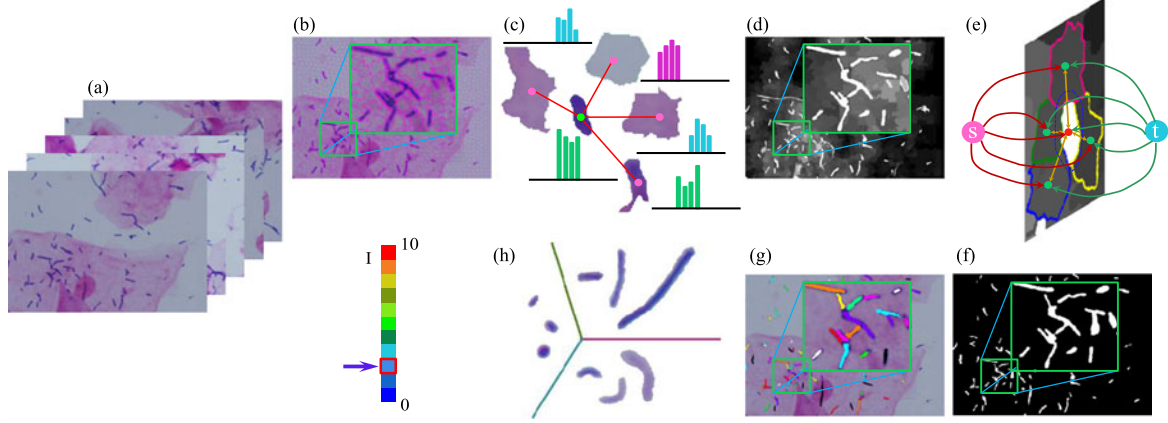


Fig. 2. Flowchart of an automatic Nugent scoring system for BV diagnosis. (a) Selecting view images from slide, (b) Grouping pixels into superpixels. (c) Computing superpixels' contrast by color information and distances weight. (d) Results for superpixels' contrast. (e) Segmenting bacteria regions by saliency cut. (f) Results for (e). (g) Splitting overlapping clumps for quantitative analysis of individual bacterium's morphotype. (h) Classifying bacterial morphotypes. (i) Diagnosing BV according to the Nugent score criterion.

superpixels. The second step is to split overlapping clumps, which is implemented by locating markers by region decomposition. Next, the evidence between pixels and markers to locate the splitting line is established. The final step starts by extracting shape features of each bacterium. Then, we use a machine learning framework to learn these features, and classify the morphotypes of each bacterium. Finally, the number of bacteria with different morphotypes is calculated, and then BV diagnosis is implemented based on the Nugent score.

A. Segment Bacteria Regions

1) Overview: Humans pay more attention to image regions with high contrast as compared to their surroundings. Regions with high contrast to its neighborhood are usually strongly evident in the human vision system. Spatial relationship is also an important element in human attention [23], [33]. However, directly introducing spatial relationship in pixel level is computationally expensive. Furthermore, it lacks robustness when there is too much noise. In this section, we introduce a region-contrast method that integrates spatial relationship into region-level contrast computation. Our method first segments the input image into regions via a superpixel algorithm, and then computes color contrast at the region level. Next, we define the saliency value by combining the space weighted value and region's contrast value. Last, we apply an MRF model in a saliency map for segmenting the bacteria regions.

2) Superpixel Generation: We use the simple linear iterative clustering approach (SLIC) [24] to generate superpixels since this method has excellent boundary adherence and high computation efficiency. In SLIC, the image is first segmented into regular grid cells. Then, local iterative k -means clustering is performed on the pixels according to the color and location information of each pixel. The iteration of k -means continues until the new centers are nearby enough with the previous ones. Finally, the isolated small clusters are merged with the largest neighbor clusters to enforce connectivity.

3) Superpixel Contrast: For a region R_p , the saliency value is computed by measuring its color contrast to all other

regions in the image, and the value is defined as

$$S(R_p) = \sum_{R_q \neq R_p} \omega(R_q) D_r(R_p, R_q), \quad (1)$$

where $\omega(R_q)$ is the weight of region R_q , which is computed by the number of pixels in R_q to emphasize the contrast to bigger regions. $D_r(R_p, R_q)$ is the color distance metric between regions R_p and R_q , which is represented by

$$D_r(R_p, R_q) = \sum_{i=1}^{N_1} \sum_{j=1}^{N_2} H(c(i)) H(c(j)) D(c(i), c(j)), \quad (2)$$

where $H(c(i))$ is the value of color $c(i)$ in the normalized color histogram when the pixel i belongs to the region R_p , N_1 , and N_2 are the number of pixels in regions R_p and R_q , respectively. $D(c(i), c(j))$ is the Euclidean distance between color value $c(i)$ and $c(j)$ in the lab color space.

To increase the effects of close region and decrease the effects of region, we integrate the spatial information by

$$S(R_p) = \sum_{R_q \neq R_p} e^{-\frac{D_s(R_p, R_q)}{\sigma^2}} \omega(R_q) D_r(R_p, R_q), \quad (3)$$

where $D_s(R_p, R_q)$ is the spatial distance between regions R_p and R_q , and it is defined as the Euclidean distance between their centroids. σ controls the strength of spatial distance weighting. A large value of σ reduces the effect of spatial weighting so that the contrast of regions would contribute more to the saliency value of the current region. This value is empirically determined as 0.6.

In addition, storing and calculating the regular histogram for each region is inefficient since the region only contains a small number of colors. Therefore, we use a sparse histogram representation for efficient computation.

4) Saliency Cut: Using a saliency map, we incorporate the spatial coherence and the global understanding for segmenting the bacteria. We implement a classical MRF and define the cost function as

$$E = \sum_{R_p \in \Omega} S(R_p) + \lambda \sum_{(R_p, R_q) \in \mathcal{E}} V(R_p, R_q), \quad (4)$$

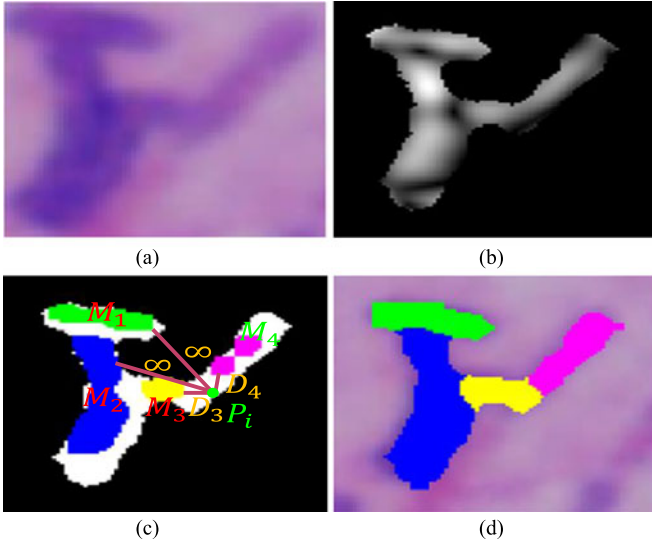


Fig. 3. Illustration of overlapping bacteria clumps splitting procedures. (a) Original clump and its location are obtained by saliency cut. (b) Difference map obtained by computing eigenvalues of Hessian matrix. (c) Decomposed markers and evidences for pixels to markers. (d) Splitting result.

where λ is the weight parameter, Ω is the regions domain, ε is the set of neighboring regions, $S(R_p)$ is the saliency value, and $V(R_p, R_q)$ is the pairwise terms defined as

$$V(R_p, R_q) = |I_{R_p} - I_{R_q}|, \quad (5)$$

where I_{R_p} and I_{R_q} are the saliency values of two neighboring regions. The MRF energy in (4) is minimized using alpha-expansions [25], [26].

B. Splitting Overlapping Clumps

Inspired by the fact that the color values inside the bacterium are different from its boundaries among touching bacteria, we propose an approach to detect the distinct features of clumps based on the eigenvalues of the Hessian matrix. The approach of overlapping clumps splitting is illustrated in Fig. 3.

1) Region Decomposition: We first transform the image to hue, saturation, value (HSV) color space, and the S channel is denoted by $S(x, y)$, which is smoothed by Gaussian kernel $G(x, y; \sigma)$ via a convolution operation, where σ is a scale parameter corresponding to the size of the target object. We empirically determined σ as 20. After Gaussian smoothing, we obtain the Hessian matrix in each pixel denoted by (x, y) via the second-order derivations of S :

$$H(x, y) = \begin{bmatrix} S_{XX} & S_{XY} \\ S_{XY} & S_{YY} \end{bmatrix}. \quad (6)$$

The local color changes are then captured by computing the eigenvalues λ_1 and λ_2 of $H(x, y)$:

$$\lambda_{1,2} = \frac{S_{XX} + S_{YY} \pm \sqrt{(S_{XX} - S_{YY})^2 + 4S_{XY}^2}}{2}. \quad (7)$$

Assuming $|\lambda_1| < |\lambda_2|$, we enhance the difference in the region clumps by

$$\lambda = \lambda_1 - \lambda_2. \quad (8)$$

We also extend the values of the difference map within $[0, 255]$ to increase the contrast in the bright and dark regions by

$$f(x, y) = \frac{255}{2} \left(1 + \frac{1}{\tan(\frac{\alpha\pi}{2})} \tan\left(\alpha\pi\left(\frac{I(x, y)}{255} - \frac{1}{2}\right)\right) \right), \quad (9)$$

$0 < \alpha < 1.$

where $I(x, y)$ is the difference map value at (x, y) , α is the parameter corresponding to the enhanced degree, and we set it as 0.7. Finally, the markers are obtained by thresholding the enhanced map f using an adaptive threshold defined as

$$Th = \tau(f_{\max} - f_{\text{med}}) + \beta f_{\text{med}} \quad (10)$$

where τ, β are adjusting parameters, and $\tau = 0.2, \beta = 1$. f_{\max} and f_{med} are the max and median values of the clumps region, respectively.

2) Associate Pixel to Markers Evidences: Once the markers are obtained, most current approaches grow markers by iterating application of geodesic dilations to the markers until it collides with other growth markers. Differing from these existing approaches, we directly define the pixel to markers' evidences. Supposing the clump region is decomposed into n markers denoted by $\{M_1, M_2, \dots, M_n\}$, where M_i is the marker corresponding to individual bacterium B_i and represented by a set of point coordinates in the marker. There remain m pixels need to be classified into the correct marker denoted as $\{P_1, P_2, \dots, P_m\}$. Next, we define a compound measure $D(P_i, M_i)$ to evaluate the relevance of P_i to M_i , which is determined by location and color distance. The location distance from P_i to M_i is defined as

$$D_g(P_i, M_i) = \min_{x \in M_i} g(P_i, x), \quad (11)$$

where $g(P_i, x)$ is the Euclidean distance $P_i - x$ when the line from P_i to x entirely resides within the clump region, and infinite (∞) when any portion of the line is outside this region. The other component in the compound measure is the color distance from P_i to M_i , which compares the difference of intensity value $I(P_i)$ at P_i with the mean intensity value $I(M_i)$ of marker region M_i and is expressed as

$$D_c(P_i, M_i) = I(P_i) - I(M_i). \quad (12)$$

Summing up $D_g(P_i, M_i)$ and $D_c(P_i, M_i)$ with a weight parameter $\xi \in [0, 1]$, the compound measure of P_i to M_i is defined as

$$D(P_i, M_i) = (1 - \xi) \frac{D_g^2(P_i, M_i)}{D_g(P_i, M_i)} + \xi \frac{D_c^2(P_i, M_i)}{D_c(P_i, M_i)}. \quad (13)$$

It should be noted that both terms are normalized within $[0, 1]$ before being weighted by ξ . We empirically set ξ to 0.7. Finally, if

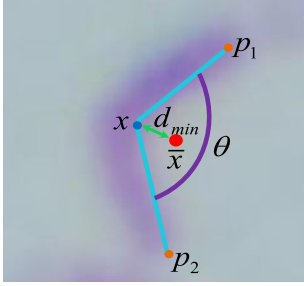
$$i = \underset{j \in \{1, 2, \dots, n\}}{\operatorname{argmin}} D(P_i, M_j), \quad (14)$$

p_i becomes an element of the marker evidence for B_j .

TABLE II

SUMMARY OF FEATURES USED TO DESCRIBE BACTERIUM MORPHOTYPES

#	Feature	Description
1	Area	The number of pixels in the region.
2	Length	The length (in pixels) of the major axis of the ellipse that has the same normalized second central moments as the region.
3	Width	The length (in pixels) of the minor axis of the ellipse that has the same normalized second central moments as the region.
4	Perimeter	The number of pixels around the boundary of the region.
5	Length–width ratio	The ratio of length and width.
6	Radius Std.	Standard deviation of radius, radius is the distance of the boundary pixel to the center of the region.
7	d_{min}	Minimal distance of the boundary pixels to the center.
8	θ	The angle between the endpoints.

Fig. 4. Illustration of minimal distance d_{min} and curvature degree θ .

C. Classifying Bacterium Morphotypes

After individual bacterium segmentation, our task is to automatically diagnose BV based on Nugent score, which depends on recognition of bacterial morphotypes. We first extract morphological features from bacteria, and then use a machine learning framework to learn these features so that we can identify different bacterial morphotypes.

1) Feature Extraction: We extract a total of eight features from each individual bacterium. The feature descriptions are summarized in Table II. Among them, five are regular morphological features, including area, length, width, perimeter, and length–width ratio to describe all three bacterial morphotypes. We also utilize the standard deviation of radius (radius Std) for *Gardnerella* morphotype since this type of bacteria has similar circular shape. Specifically, the radius Std \hat{d} is defined as

$$\hat{d} = \sqrt{\frac{1}{N} \sum_{i=1}^N (d_i - \bar{d})^2}, \quad (15)$$

where N is the number of bacterium boundary pixels, d_i is the distance of the boundary pixel i to bacterium centroid, and \bar{d} is the mean distance of d_i . Furthermore, we also design two new features: d_{min} and θ to accurately characterize *Mobiluncus* morphotypes, which are shown in Fig. 4. We define d_{min} as

$$d_{min} = \text{sign}(f(\bar{x})) \min_{x \in E} x - \bar{x}, \quad (16)$$

where E is the set of all boundary pixels, \bar{x} is the centroid of the bacterium region, when it is located in the bacterium re-

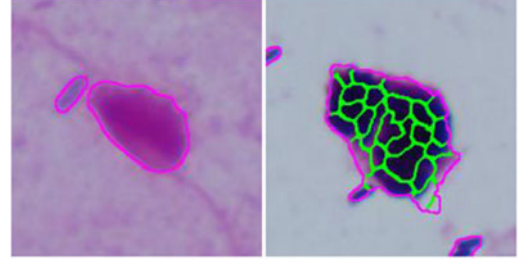


Fig. 5. Illustration of two kinds of segmentation error.

gion, $f(\bar{x}) > 0$, otherwise, $f(\bar{x}) \leq 0$, and $x - \bar{x}$ is the Euclidean distance between boundary pixel x and \bar{x} . This promising feature is used to describe the curve shape. Another intuitive feature to describe this shape is the curvature degree: θ . In order to quantify the curvature degree, we determine the closest boundary pixel x to the centroid \bar{x} , and then find the endpoints p_1 and p_2 using the maximum distance principle. Finally, θ is computed as

$$\theta = \frac{\vec{l}(x, p_1) \cdot \vec{l}(x, p_2)}{|\vec{l}(x, p_1)| |\vec{l}(x, p_2)|}, \quad (17)$$

where $\vec{l}(x, p)$ is the direction of line from x to p . Finally, we suppress large value features dominating those in a small value by normalizing them within $[0, 1]$.

2) Morphotypes Learning: We use an Adaptive Boosting (AdaBoost) machine learning framework [27] to learn the bacterium descriptors and characterize each morphotype based on the above-defined features. AdaBoost is a meta-algorithm, which can be used in conjunction with many different weak classifiers to improve their performance. Specifically, we use Gentle AdaBoost [28] since it is a more robust and stable version of AdaBoost model [29], and it has been one of the most practically efficient boosting algorithms.

In our experiments, we train five binary classifiers, because there are two types of segmentation errors. Fig. 5 shows the two segmentation errors. One is the large region usually including nucleus or leukocyte, another error is that these large region is split into various small regions. The generated errors reserve nonbacteria regions in the segmentation result, which is able to ensure all the bacteria regions can be detected. Each specific binary classifier assigns each candidate region either the “class” or “nonclass” label for each morphotype. The outcomes of the five binary classifiers are combined into one multilabel classifier by choosing the component label with the highest confidence.

3) BV Diagnosis: BV diagnosis is implemented at the slide level, which is more relevant for practical diagnosis. One issue of BV diagnosis is the number of view images sampled from the slide. The second issue would be how to choose these images. In clinic, microscopists select images from the slide based on their experience, and they increase the number of view images until they can give the diagnosis result. In this section, we refer to how experts manually classify them. Since experts usually need ten images in each slide to diagnose BV, we set the image number as ten. Furthermore, to reduce artifact we randomly choose images for each slide. After the images have been chosen, we implement our algorithm to segment each

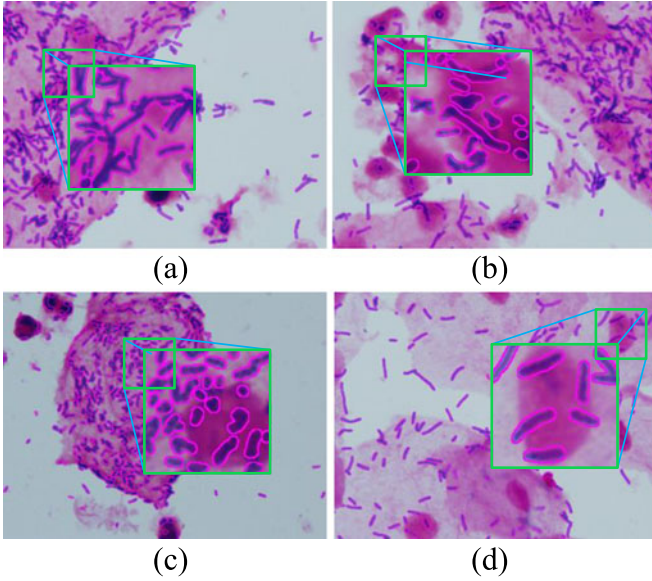


Fig. 6. Segmentation results of bacteria regions.

bacterium and determine its morphotypes. Finally, according to the average number of bacteria in these ten images, BV diagnosis is implemented using Nugent score criterion. The BV patient is determined by the Nugent score in the range of 7 and 10.

III. EXPERIMENTAL RESULTS

A. Clinical Data Collection

The data set is collected from the Department of Laboratory, Shenzhen Sixth People's Hospital, Shenzhen, China, in the year of 2013, which contains 105 women's slides of aged from 18 to 50 and all slides are processed by Gram stain. Among them, 51 slides were confirmed as normal vaginal flora, 42 slides as altered vaginal flora, and 12 slides as BV. The golden standard of all slides are provided by experts.

In general, a typical slide contains about $100k \times 100k$ pixels with an Olympus BX43 microscope equipped with $100\times$ objective. The clinicians usually choose about 10–20 microscope images comprised about $1k \times 1k$ pixels to diagnose BV. We collected an average of 105 microscope images for each slide to construct our dataset to ensure sufficient data are used, and the image specifications are 24 bit RGB channels with a resolution of 1360×1024 pixels.

It should be noted that all the materials used in this paper have been approved by the Ethics Committee of the Sixth People's Hospital of Shenzhen. The Human Subjects Review Committee of Shenzhen University also reviewed and approved the study protocol and consent documents. We also have the written permission obtained from each participant.

B. Results for Bacteria Regions Segmentation

1) *Qualitative Results*: Qualitative results for 4 of the 105 different slides are illustrated in Fig. 6, which reflect the effectiveness of our model. Fig. 6(A) shows that our method

can accurately segment overlapping bacteria regions even with high overlapping degree. Fig. 6(B) and (C) illustrates that our method has excellent edge capture ability under the unfavorable conditions, such as illumination variances, dye concentration, and uneven dying. Fig. 6(D) shows that good segmentation performance is achieved even under low contrast conditions, such as air drying, excessive blood, mucus, nuclei, cytoplasm, and leukocyte. It is clear that our method has good performance with images with inconsistent staining, poor contrast, and touching bacteria.

2) *Quantitative Results*: We randomly choose 2000 bacteria regions for quantitative evaluation. The boundaries of these regions have been manually annotated. Note that the annotation of real microscope images is time-consuming and potentially error-prone, which limits the feasibility to evaluate at image level. Quantitative performance is then assessed using the correct segmentation ratio that defined as $Acc = (A \cap B)/(A \cup B)$.

Table III summarizes the means and standard deviations of segmentation accuracy. As shown in Table III, the high segmentation accuracy and low standard deviations of the proposed method demonstrates its effectiveness and robustness.

C. Results for Overlapping Clumps Splitting

1) *Qualitative Results*: Some representative splitting results are displayed in Fig. 7, in which each pair represents one individual clump and the splitting result. We can see that when the number of overlapping bacteria is 2–4, the proposed approach performs well even though there are a wide range of bacterial sizes and various overlapping types. Furthermore, when the number of overlapping bacteria is above 4, the overall segmentation performances are acceptable though the accuracy is lower compared with the former cases. In general, when the bacteria number is less than 10, our method produces good result in these overlapping cases.

2) *Quantitative Results*: To evaluate the splitting accuracy, we use three types of errors: undersplitting, oversplitting, and insufficient errors. The undersplitting error occurs when the algorithm does not place a boundary between a pair of overlapping bacteria. The oversplitting error occurs when the algorithm places a boundary within a single bacterium. For example, for a specific region, the bacterial number is 3, but it is split into 4 or more bacteria. The insufficient error occurs when the splitting algorithm does not correctly place the boundary between a pair of touching bacteria. We quantify the error by computing the mean dice similarity coefficient (DSC) defined as follows:

$$DSC = \frac{1}{N} \sum_{i=1}^N \frac{A_i \cap B_i}{A_i \cup B_i}, \quad (18)$$

where N is the bacteria number, A is the manual annotation, and B is the splitting result. We define the insufficient error as $DSC < 0.7$.

We randomly choose 3000 overlapping bacteria regions including 6 overlapping types according to the object number, and each type has 500 samples. The quantitative evaluation results are tabulated in Table IV. It can be seen that the

TABLE III
QUANTITATIVE EVALUATION OF THE SEGMENTATION RESULTS

	Lactobacillus Morphotypes		Gardnerella Morphotypes		Mobiluncus Morphotypes		Mixed	
	Region Number	$\mu_{Acc} \pm \sigma_{Acc}$	Region Number	$\mu_{Acc} \pm \sigma_{Acc}$	Region Number	$\mu_{Acc} \pm \sigma_{Acc}$	Region Number	$\mu_{Acc} \pm \sigma_{Acc}$
1 bacterium	244	0.83 ± 0.08	261	0.77 ± 0.11	86	0.73 ± 0.08	N/A	N/A
2–5 bacteria	197	0.81 ± 0.13	272	0.76 ± 0.13	14	0.71 ± 0.14	121	0.79 ± 0.11
6–10 bacteria	172	0.79 ± 0.11	183	0.78 ± 0.17	N/A	N/A	96	0.77 ± 0.15
>10 bacteria	156	0.77 ± 0.19	143	0.79 ± 0.15	N/A	N/A	55	0.74 ± 0.21
Average	769	0.80 ± 0.12	859	0.77 ± 0.14	100	0.73 ± 0.10	272	0.77 ± 0.17

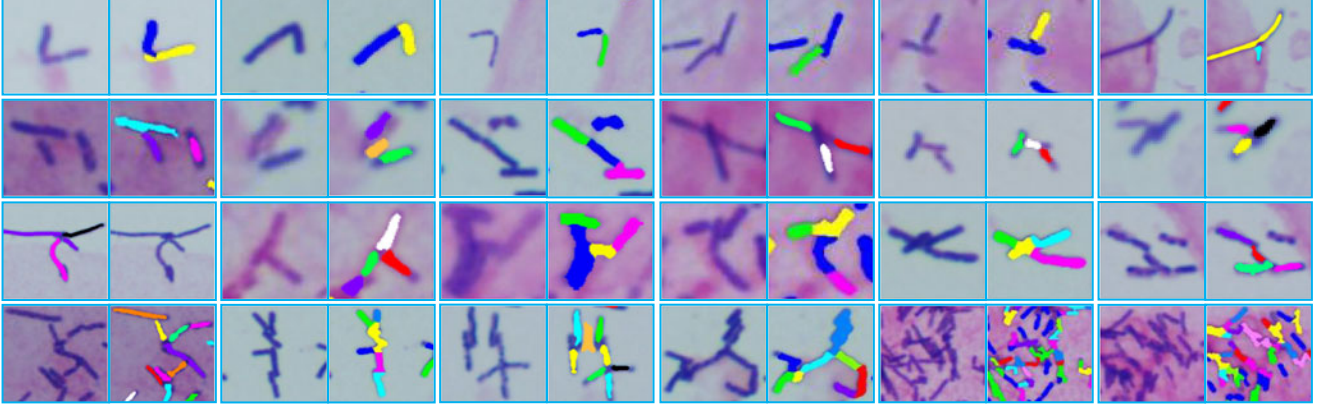


Fig. 7. Examples of splitting overlapping bacteria clumps. For each pair, right image corresponds to splitting result for each overlapping bacteria clump, and the left image is the original image. Note that some images have been resized for improved visibility.

TABLE IV
QUANTITATIVE EVALUATION OF THE SPLITTING RESULTS

Bacteria Number	Correct Split	Undersplit	Oversplit	Insufficient Error
2	467	12	17	4
3	438	17	26	19
4	401	29	44	26
5	372	41	62	25
6–10	314	53	66	67
>10	271	57	74	98

quantitative and qualitative results are consistent. When the number of touching bacteria is 2–4, the correctly splitting accuracy is 87.1%. When the number of touching bacteria is 5–10, the accuracy is 68.6%, and when the bacteria number is beyond 10, the accuracy is 54.2%.

D. Results for Morphotypes Learning

For the learning task, when the feature has obtained, the learning method determines the final learning accuracy. In this section, different classifiers are tested, including support vector machine (SVM) [30], back propagation neural network (BP NN) [31], real AdaBoost [29], and modest AdaBoost [32]. SVM is based on the typical statistical learning theory and can overcome the overfitting problems. By structure risk minimization principle, SVM has achieved excellent performance in numerous applications. In our experiment, we use a one-against-all

strategy for the multiclass bacteria morphotypes recognition task. We train five SVM classifiers for each class by assuming the training set of this class as positive samples and those remaining as negative samples. In the testing stage, each testing image returns the label with the highest confidence. Meanwhile, different kernels were tested, including linear kernel (LK), intersection kernel (IK), Jensen–Shannon kernel (JSK), and χ^2 kernel (χ^2 K).

BPNN is one of the most popular network models for learning various input–output mapping relationships. The same learning strategy as SVM is implemented for evaluating learning methods objectively. In addition, Real AdaBoost and Modest AdaBoost classifiers are also chosen for comparison of the learning approaches. Real AdaBoost is a generalization of a basic AdaBoost algorithm, and it is treated as a “hardcore” boosting algorithm. Modest AdaBoost is a regularized AdaBoost, which have better generalization capability and resistance to overfitting. The AdaBoost based algorithms have two parameters: the maximal depth (d) for tree learners, and the maximal iteration number (I). In our experiment, $d = 3$ and $I = 200$.

To obtain a reasonable learning result, we performed fivefold cross-validation trials. We choose a total of 4000 manually labeled bacteria regions, and each class has 800 samples. In each trial, we randomly divide 80% of labeled bacteria into the training set, 20% of the remaining into the test set. We measure the mean and standard deviation of the classification error (the percentage of the number of bacteria regions recognized incorrectly in the test set) across the five trials. The statistic results

TABLE V
CLASSIFICATION PERFORMANCE AMONG DIFFERENT CLASSIFIERS

SVM		BP NN		AdaBoost	
Kernel	Error Rate(%)	Structure	Error Rate (%)	scheme	Error Rate (%)
LK	36.9 ± 6.4	20-20-1	20.3 ± 8.7	Real	12.7 ± 2.2
IK	16.7 ± 5.8	20-60-1	21.1 ± 9.4	Gentle	12.3 ± 1.3
JSK	12.9 ± 4.2	60-20-1	21.6 ± 8.6	Modest	21.6 ± 1.9
χ^2 K	14.4 ± 6.3	40-40-1	19.6 ± 8.4	N/A	N/A

of various classifiers are shown in Table V. In SVM classifiers, JSK achieves the best result, but all SVM classifiers have high standard deviation. The BP NN classifiers get the worst classification performance and the highest standard deviation. Meanwhile, the AdaBoost machine learning framework has the lowest standard deviation, and the Gentle AdaBoost obtains the best performances in terms of the error rate.

E. Results for BV Diagnosis

To evaluate the performance of BV diagnosis, we only use ten images of each slide to diagnose BV. In clinical practices, the number of used image varies depending on the experience of the implementers and the complexity of slide. For example, some slides are difficult to diagnose, implementers maybe need more than ten images for obtaining the accurate results. The ten images are selected randomly to evaluate the robustness of the proposed method. In clinical practices, the number of used image varies with the experience of implementers and the complexity of slides. For example, some slides are difficult to diagnose BV, and the implementer may need more than ten images to obtain the accurate results. Also, we randomly select these images for evaluating the robustness of the proposed method, which is quite important for an automatic tool. In fact, in clinical practices, implementers choose the images which can boost their diagnosis efficiency and accuracy, and ignore these images are hard to distinguish. In this section, the proposed method, human readers, microscopists, and experts are only given ten randomly selected images to diagnose BV for objective evaluation. (The human reader in this study only receives the guidance from experts, the microscopist have more than 3 years of clinical practice, whereas the expert has more than 10 years of clinical practice.)

In addition, the slides are split into three parts according to the Nugent score: 1) normal vaginal flora (Nugent score: 0–3); 2) altered vaginal flora (Nugent score: 4–6); and 3) BV (Nugent score: 7–10). We have 51 normal vaginal flora slides, 42 altered vaginal slides, and only 12 BV slides in total. To address the problem of data imbalance, we adopt the bootstrapping method [37], which is the most used technique in statistics to address the problem of limited samples. We randomly choose ten microscope images in the remaining images in each BV slide, and we repeat this procedure twice to expand the BV slides to 36 in total.

Table VI shows the results of the performance produced by different methods. The best and worst performance of human readers and microscopists are eliminated to remove any bias occurred. We can see from the table that the experts achieve the

TABLE VI
BV DIAGNOSIS RESULTS IN SLIDE-LEVEL

	Normal Vaginal Flora	Altered Vaginal Flora	BV	Sensitivity	Specificity	Average Accuracy
N score	0–3	4–6	7–10	N/A	N/A	N/A
Golden Standard	51	42	12×3	N/A	N/A	N/A
Our method	43	38	21	58.3%	87.1%	79.1%
Human readers	46	24	22	61.1%	75.3%	71.3%
Microscopists	50	31	27	75.0%	87.1%	83.7%
Experts	50	37	30	83.3%	93.5%	90.7%

best diagnosis accuracy of 90.7%, and the percentage of diagnosis BV correctly is also 90.7%. “Normal vaginal flora” and “Altered vaginal flora” are not regarded as BV, and they cannot be diagnosed totally correctly for each slide by all methods. Therefore, the percentage of correct BV diagnosis is higher than the “Average accuracy” shown in the Table VI. To avoid confusion of these two values, in the following, the percentage of correct BV diagnosis is indicated in the round brackets. In fact, the automatic method achieves an accuracy of 79.1% (86.0%), which is comparable to the microscopists with the accuracy of 83.7% (86.8%), but it is superior to the Human readers with the accuracy of 71.3% (79.8%). Moreover, we achieve the lowest accuracy in normal bacteria, and there are two main explanations for this: 1) It is easy to distinguish normal bacteria by human eyes due to obvious morphotypes, such as large size, length, and width; 2) it is challenging for the automatic algorithm when the bacteria are heavily overlapped, and these bacteria are similar with Gardnerella morphotype due to the splitting error. However, the diagnosis accuracy of altered vaginal flora obtained by the proposed method is even higher than that of the experts. Obviously, the statistical results demonstrate that the proposed method achieves a promising accuracy of BV diagnosis.

IV. DISCUSSIONS

From Table IV, we can see that when the bacteria number is 6–10, the results obtained by the proposed method is only 68.6%. Considering the variations of bacteria’ morphotypes and the overlapping types, the accuracy is still acceptable. However, when the bacteria number is beyond 10, the accuracy is only 54.2%. In fact, the segmentation accuracy is not high enough. The main reason is that the ways of overlapping are too complicated, splitting these overlapping bacteria is a challenging task, even for the experts, getting high performance in these challenging conditions is also extremely difficult.

As illustrated in Table V, BP NN obtained not only the worst learning error, but also the highest standard deviation. The main reason is that the initialization process of BP NN is stochastic. Meanwhile, the AdaBoost machine learning framework has the lowest standard deviation, and the Gentle AdaBoost produces the best performances. The primary explanation is that Gentle AdaBoost is more robust and resistant than other classifiers.

As for the BV diagnosis, we achieve the lowest accuracy in “Normal vaginal flora” and “BV.. The inaccurate diagnosis result mainly happens on patients with Nugent score below 2

TABLE VII

BV DIAGNOSIS RESULTS OF THE PROPOSED METHOD WITH VIEW IMAGES SELECTED BY HUMAN READERS, MICROSCOPISTS AND EXPERTS, AND THESE RESULTS ARE ALSO COMPARED WITH THE RESULTS PRODUCED BY PROPOSED METHOD WHEN VIEW IMAGES SELECTED BY RANDOMLY

	Sensitivity		Specificity		Average Accuracy	
	Results	Improved	Results	Improved	Results	Improved
Human readers	66.7%	14.4%	89.2%	2.4%	86.7%	9.6%
Microscopists	66.7%	14.4%	89.2%	2.4%	86.7%	9.6%
Experts	75.0%	28.6%	90.3%	3.7%	88.6%	12.0%

or above 8. In both cases, images mainly contain *Lactobacillus* or *Gardnerella* morphotypes with heavy bacteria overlapping. Human can distinguish single type of bacteria easily by human eyes even when the bacteria are heavily overlapped because they can utilize contextual information for this task. However, it is challenging for the automatic algorithm to capture the contextual information, especially the relationship among different images. Actually, contextual information plays an important role in human vision recognition and understanding system [38]. The ability to capture contextual information mainly depends on the experience of disease diagnosis. For this reason, it is really challenging for artificial machine to beat the experts in the BV diagnosis.

In fact, the slide-level recognition for BV diagnosis is full of challenges. Therefore, even the experts are unlikely to achieve 100% accuracy. In this case, implementers usually add the number of images from slide or use other ways to diagnose BV. To increase the accuracy of BV diagnosis, implementers usually add the number of view images from slide in the clinical practices. The added view images have a close relationship with the previous view images. However, our proposed method has difficulty in quantifying such internal relationships to increase BV diagnosis accuracy. If the view images are selected by implementers in clinical practices, the proposed method will become more powerful using this internal correlation, which also renders the implementers to accept the proposed automatic system due to the increased accuracy. Therefore, we perform another experiment based on the view images selected by five human readers, five microscopists, and five experts from our 105 slides. They all select view images on each slide independently. Table VII shows the averaged results from each group. We can see that the method based on view images selected from implementers get better performance especially in terms of sensitivity than that with randomly selected images. By combining the implementers' selection, our proposed method can effectively boost BV diagnosis accuracy, which shows the potential clinical application of our proposed method as well.

In addition, although the average running time per microscope image with 1360×1024 pixels is around 30 s (code implemented in MATLAB and on a 4 core PC, 4 GB RAM, 3.19 GHz CPU), it is still possible to further reduce the processing time by more powerful CPUs. And the overlapping clumps splitting processes and the saliency value computation in each superpixel can be executed in parallel.

Finally, in our future research direction, we will incorporate the shape constraints and develop a shape inference method to enhance the splitting performance. It shall explore the application of a discriminative learning method to characterize features with a suitable classifier in order to identify the most informative feature for BV diagnosis. Furthermore, the optimal saliency computation is also possible to boost the performance.

V. CONCLUSIONS

In this paper, we developed an automatic algorithm for BV diagnosis. We explored the human biological vision-based method to segment the bacteria regions. We also proposed a method to split the overlapping bacteria, which have the unsmoothed boundaries, and the size variation among these bacteria is wide. Finally, we diagnosed BV based on recognizing bacterial morphotypes, and the proposed method allows BV diagnosis to be more effective and efficient.

REFERENCES

- [1] A. Esber *et al.*, "Risk of bacterial vaginosis among women with herpes simplex virus type 2 infection: A systematic review and meta-analysis," *J. Infect. Dis.*, vol. 12, no. 1, pp. 1–10, 2015.
- [2] C. R. Cohen *et al.*, "Bacterial vaginosis associated with increased risk of female-to-male HIV-1 transmission: A prospective cohort analysis among African couples," *PLoS Med.*, vol. 9, no. 6, pp. e1001251.1–e1001251.9, 2012.
- [3] Y. Turovskiy, K. Sutyak-Noll, and M. L. Chikindas, "The aetiology of bacterial vaginosis," *J. Appl. Microbiol.*, vol. 110, pp. 1105–1128, 2011.
- [4] R. P. Nugent, A. K. Marijane, and L. H. Sharon, "Reliability of diagnosing bacterial vaginosis is improved by a standardized method of Gram stain interpretation," *J. Clin. Microbiol.*, vol. 29, pp. 297–301, 1991.
- [5] L. F. Handfield, B. Strome, Y. T. Chong, and A. M. Moses, "Local statistics allow quantification of cell to cell variability from high-throughput microscope images," *Bioinformatics*, vol. 31, no. 6, pp. 940–947, 2015.
- [6] S. Dimopolous, E. M. Christian, R. Fabian, and S. Joerg, "Accurate cell segmentation in microscopy images using membrane patterns," *Bioinformatics*, vol. 30, no. 18, pp. 2644–2651, 2014.
- [7] N. Otsu, "A threshold selection method from gray-level histograms," *IEEE Trans. Syst., Man, Cybern.*, vol. 9, no. 1, pp. 62–66, Jan. 1979.
- [8] O. D. Trier and A. K. Jain, "Goal-directed evaluation of binarization methods," *IEEE Trans. Pattern Anal. Mach. Intell.*, vol. 17, no. 12, pp. 1191–1201, Dec. 1995.
- [9] L. Vincent and P. Soille, "Watersheds in digital spaces: An efficient algorithm based on immersion simulations," *IEEE Trans. Pattern Anal. Mach. Intell.*, vol. 13, no. 6, pp. 583–598, Jun. 1991.
- [10] L. Gorelick *et al.*, "Prostate histopathology learning tissue component histograms for cancer detection and classification," *IEEE Trans. Med. Imaging*, vol. 32, no. 10, pp. 1804–1818, Oct. 2013.
- [11] Y. Y. Xu, F. Yang, Y. Zhang, and H. B. Shen, "Bioimaging-based detection of mislocalized proteins in human cancers by semi-supervised learning," *Bioinformatics*, vol. 31, no. 7, pp. 1111–1119, 2015.
- [12] Y. Xu, J. Y. Zhu, E. I. Chang, M. Lai, and Z. W. Tu, "Weakly supervised histopathology cancer image segmentation and classification," *Med. Image Anal.*, vol. 18, no. 3, pp. 591–604, 2014.
- [13] G. E. Hinton, "Learning multiple layers of representation," *Trends Cogn. Sci.*, vol. 11, no. 10, pp. 428–434, 2007.
- [14] Y. Y. Song, L. Zhang, S. P. Chen, D. Ni, B. Y. Lei, and T. F. Wang, "Accurate segmentation of cervical cytoplasm and nuclei based on multi-scale convolutional network and graph partitioning," *IEEE Trans. Biomed. Eng.*, vol. 62, no. 10, pp. 2421–2433, Oct. 2015. DOI: 10.1109/TBME.2015.2430895.
- [15] T. F. Chan and A. V. Luminita, "Active contours without edges," *IEEE Trans. Image Process.*, vol. 10, no. 2, pp. 266–277, Feb. 2001.
- [16] J. Cheng and J. Rajapakse, "Segmentation of clustered nuclei with shape markers and marking function," *IEEE Trans. Biomed. Eng.*, vol. 56, no. 3, pp. 741–748, Mar. 2009.

- [17] H. G. Yang and N. Ahuja, "Automatic segmentation of granular objects in images: Combining local density clustering and gradient-barrier watershed," *Pattern Recogn.*, vol. 47, no. 6, pp. 2266–2279, 2014.
- [18] S. Ali and M. Anant, "An integrated region-, boundary-, shape-based active contour for multiple object overlap resolution in histological imagery," *IEEE Trans. Med. Imag.*, vol. 31, no. 7, pp. 1448–1460, Jul. 2012.
- [19] Z. Lu, C. Gustavo, and P. B. Andrew, "An improved joint optimization of multiple level set functions for the segmentation of overlapping cervical cells," *IEEE Trans. Image Process.*, vol. 24, no. 4, pp. 1261–1272, Apr. 2015.
- [20] T. Janssens, L. Antanas, S. Derde, I. Vanhorebeek, G. Van, and F. Guiza, "Charisma: An integrated approach to automatic H&E-stained skeletal muscle cell segmentation using supervised learning and novel robust clump splitting," *Med. Image Anal.*, vol. 17, no. 8, pp. 1206–1219, 2013.
- [21] H. Kong, G. Metin, and B. B. Kamel, "Partitioning histopathological images an integrated framework for supervised color-texture segmentation and cell splitting," *IEEE Trans. Med. Imag.*, vol. 30, no. 9, pp. 1661–1677, Sep. 2011.
- [22] P. Quelhas, M. Monica, M. M. Ana, and C. Aurelio, "Cell nuclei and cytoplasm joint segmentation using the sliding band filter," *IEEE Trans. Med. Imag.*, vol. 29, no. 8, pp. 1463–1473, Aug. 2010.
- [23] M. M. Cheng, N. J. Mitra, X. L. Huang, Philip H. S. Torr, and S. M. Hu, "Salient object detection and segmentation," *IEEE Trans. Pattern Anal. Mach. Intell.*, vol. 37, no. 3, pp. 569–582, DOI: 10.1109/TPAMI.2014.2345401.
- [24] R. Achanta, A. Shaji, K. Smith, A. Lucchi, P. Fua, and S. Susstrunk, "SLIC superpixels compared to state-of-the-art superpixel methods," *IEEE Trans. Pattern Anal. Mach. Intell.*, vol. 34, no. 11, pp. 2274–2282, Nov. 2012.
- [25] Y. Boykov and V. Kolmogorov, "An experimental comparison of min-cut/max-flow algorithms for energy minimization in vision," *IEEE Trans. Pattern Anal. Mach. Intell.*, vol. 26, no. 9, pp. 1124–1137, Sep. 2004.
- [26] Y. Boykov, O. Veksler, and R. Zabih, "Fast approximate energy minimization via graph cuts," *IEEE Trans. Pattern Anal. Mach. Intell.*, vol. 23, no. 11, pp. 1222–1239, Nov. 2001.
- [27] Y. Freund and E. S. Robert, "A short introduction to boosting," *J. Japan Soc. Artif. Intell.*, vol. 14, no. 5, pp. 771–780, 1999.
- [28] J. Friedman, H. Trevor, and T. Robert, "Additive logistic regression: A statistical view of boosting," *Annu. Statist.*, vol. 38, no. 2, pp. 337–374, 2000.
- [29] E. Schapire and S. Yoram, "Improved boosting algorithms using confidence rated predictions," *Mach. Learn.*, vol. 37, no. 3, pp. 297–336, 1999.
- [30] V. N. Vapnik, "An overview of statistical learning theory," *IEEE Trans. Neural Netw.*, vol. 10, no. 5, pp. 988–999, Sep. 1999.
- [31] E. Rumelhart, E. H. Geoffrey, and J. W. Ronald, "Learning representations by back propagating errors," *Nature*, vol. 323, no. 9, pp. 533–536, 1986.
- [32] Y. L. Wang *et al.*, "A new method for solving overfitting problem of gentle AdaBoost," in *Proc. 5th Int. Conf. Graphic Image Process.*, 2014, pp. 90691P.1–90691P.6.
- [33] P. F. Felzenszwalb, "Efficient graph-based image segmentation," *Int. J. Comput. Vis.*, vol. 59, pp. 167–181, 2004.
- [34] L. Zhang *et al.*, "Automation-assisted cervical cancer screening in manual liquid-based cytology with Hematoxylin and Eosin staining," *Cytom. Part A*, vol. 85A, pp. 214–230, 2014.
- [35] J. Chang *et al.*, "Automated tuberculosis diagnosis using fluorescence images from a mobile microscope," in *Proc. 15th Int. Conf. Med. Image Comput. Comput.-Assisted Intervention*, 2012, pp. 345–352.
- [36] H. Verstraelen and A. Swidsinaki, "The biofilm in bacterial vaginosis: Implications for epidemiology, diagnosis and treatment," *Curr. Opin. Infect. Dis.*, vol. 26, no. 1, pp. 86–89, 2013.
- [37] D. M. Hills and J. J. Bull, "An empirical test of bootstrapping as a method for assessing confidence in phylogenetic analysis," *Syst. Bio.*, vol. 42, no. 2, pp. 182–192, 1993.
- [38] A. Oliva and A. Torralba, "The role of context in object recognition," *Trends Cogn. Sci.*, vol. 11, no. 12, pp. 520–527, 2007.



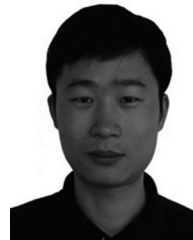
Youyi Song received the B.Eng. degree in medical information engineering from Sichuan University, Sichuan, China, in 2013. He is currently working toward the Master's degree in the School of Biomedical Engineering, Shenzhen University, Guangdong, China.

His research interests include image segmentation, machine learning, and shape analysis.



Liang He received the Master's degree from Guangdong Medical University, Guangdong, China, in 2000.

He is a Chief Technician in the Department Of Clinical Laboratory, Yunnan Tumor Hospital, Yunnan, China. His research interests include micro-ecology and clinical laboratory diagnosis.



Feng Zhou received the Bachelor's degree from Ningbo University, Ningbo, China, in 2005, and the M.S. degree from Zhejiang University, Hangzhou, China, in 2007, both in electronic engineering, and the Ph.D. degrees in human factors engineering from Nanyang Technological University, Singapore, in 2011, and in mechanical engineering from the Georgia Institute of Technology, Atlanta, GA, USA, in 2014.

He is currently an Assistant Professor at the Department of Industrial and Manufacturing Systems Engineering, The University of Michigan, Dearborn, MI, USA. His current research interests include engineering design, human factors engineering, human-computer interaction, and user research.



Siping Chen received the Ph.D. degree in biomedical engineering from Xi'an Jiaotong University, Shaanxi, China, in 1987.

He is currently a Professor in the School of Biomedical Engineering, and the Director of National-Regional Key Technology Engineering Laboratory for Medical Ultrasound, Shenzhen University, China. His research interests include ultrasound imaging, digital signal processing, and pattern recognition.



Dong Ni received the Ph.D. degree in computer science and engineering from the Chinese University of Hong Kong, Hong Kong, in 2009.

He is currently an Associate Professor in the School of Biomedical Engineering, Shenzhen University, China. His research interests include ultrasound image analysis, image guided surgery, and pattern recognition.



Baiying Lei received the M.Eng. degree in electronics science and technology from Zhejiang University, Zhejiang, China, in 2007, and the Ph.D. degree from Nanyang Technological University, Singapore, in 2013.

She is currently with the School of Biomedical Engineering, Shenzhen University, China. Her current research interests include medical image analysis, machine learning, digital watermarking, and signal processing.



Tianfu Wang received the Ph.D. degree in biomedical engineering from Sichuan University, Sichuan, China, in 1997.

He is currently a Professor in the School of Biomedical Engineering, Shenzhen University, China. His research interests include ultrasound image analysis, medical image processing, pattern recognition, and medical imaging.